Multi-channel SPR biosensor based on PCF for multi-analyte sensing applications

R. Otupiri,[1] E. K. Akowuah,[2] and S. Haxha[3,*]

[1]*Department of Electrical & Electronic Eng., Kwame Nkrumah University of Science and Technology, Ghana*
[2]*Department of Computer Eng., Kwame Nkrumah University of Science and Technology, Ghana*
[3]*Department of Computer Science and Technologies, University of Bedfordshire, University Square, Luton, Bedfordshire, LU1 3JU, UK*
[*]*Shyqyri.Haxha@beds.ac.uk*

Abstract: This paper presents a theoretical investigation of a novel holey fiber (Photonic Crystal Fiber (PCF)) multi-channel biosensor based on surface plasmon resonance (SPR). The large gold coated micro fluidic channels and elliptical air hole design of our proposed biosensor aided by a high refractive index over layer in two channels enables operation in two modes; multi analyte sensing and self-referencing mode. Loss spectra, dispersion and detection capability of our proposed biosensor for the two fundamental modes (HE_{11}^{x} and HE_{11}^{y}) have been elucidated using a Finite Element Method (FEM) and Perfectly Matching Layers (PML).

OCIS codes: (130.6010) Sensors; (240.6680) Surface plasmons; (060.2370) Fiber optics sensors; (130.3120) Integrated optics devices.

References and links

1. Y. Wan, Z. Zheng, Z. Lu, J. Liu, and J. Zhu, "Self-referenced sensing based on a waveguide-coupled surface plasmon resonance structure for background-free detection," Sens. Actuators B Chem. **162**(1), 35–42 (2012).
2. A. K. Sharma, R. Jha, and B. Gupta, "Fiber-optic sensors based on surface plasmon resonance: a comprehensive review," Sensors Journal, IEEE **7**(8), 1118–1129 (2007).
3. W. Qin, S. Li, Y. Yao, X. Xin, and J. Xue, "Analyte-filled core self-calibration microstructured optical fiber based plasmonic sensor for detecting high refractive index aqueous analyte," Opt. Lasers Eng. **58**, 1–8 (2014).
4. B. Sun, M.-Y. Chen, J. Zhou, and Y.-K. Zhang, "Surface plasmon induced polarization splitting based on dual-core photonic crystal fiber with metal wire," Plasmonics **8**(2), 1253–1258 (2013).
5. H. W. Lee, M. A. Schmidt, P. Uebel, H. Tyagi, N. Y. Joly, M. Scharrer, and P. S. J. Russell, "Optofluidic refractive-index sensor in step-index fiber with parallel hollow micro-channel," Opt. Express **19**(9), 8200–8207 (2011).
6. Y. Zhang, C. Zhou, L. Xia, X. Yu, and D. Liu, "Wagon wheel fiber based multichannel plasmonic sensor," Opt. Express **19**(23), 22863–22873 (2011).
7. A. Hassani and M. Skorobogatiy, "Design criteria for microstructured-optical-fiber-based surface-plasmon-resonance sensors," JOSA B **24**(6), 1423–1429 (2007).
8. B. Gauvreau, A. Hassani, M. Fassi Fehri, A. Kabashin, and M. A. Skorobogatiy, "Photonic bandgap fiber-based Surface Plasmon Resonance sensors," Opt. Express **15**(18), 11413–11426 (2007).
9. X. Yu, Y. Zhang, S. Pan, P. Shum, M. Yan, Y. Leviatan, and C. Li, "A selectively coated photonic crystal fiber based surface plasmon resonance sensor," J. Opt. **12**(1), 015005 (2010).
10. N. Takeyasu, T. Tanaka, and S. Kawata, "Metal deposition deep into microstructure by electroless plating," Jpn. J. Appl. Phys. **44**(35), L1134–L1137 (2005).
11. P. J. Sazio, A. Amezcua-Correa, C. E. Finlayson, J. R. Hayes, T. J. Scheidemantel, N. F. Baril, B. R. Jackson, D.-J. Won, F. Zhang, E. R. Margine, V. Gopalan, V. H. Crespi, and J. V. Badding, "Microstructured optical fibers as high-pressure microfluidic reactors," Science **311**(5767), 1583–1586 (2006).
12. J. A. Harrington, "A review of IR transmitting, hollow waveguides," Fiber and Integrated Optics **19**(3), 211–227 (2000).
13. I. Konidakis, G. Zito, and S. Pissadakis, "Silver plasmon resonance effects in AgPO 3/silica photonic bandgap fiber," Opt. Lett. **39**(12), 3374–3377 (2014).
14. J. N. Dash and R. Jha, "SPR Biosensor Based on Polymer PCF Coated With Conducting Metal Oxide," IEEE Photon. Technol. Lett. **26**(6), 595–598 (2014).
15. Y. Zhao, Z.- Deng, and J. Li, "Photonic crystal fiber based surface plasmon resonance chemical sensors," Sens. Actuators B Chem. **202**, 557–567 (2014).

#235087 - $15.00 USD Received 23 Feb 2015; revised 13 Apr 2015; accepted 15 Apr 2015; published 5 Jun 2015

16. S. Pearce, M. Charlton, J. Hiltunen, J. Puustinen, J. Lappalainen, and J. Wilkinson, "Structural characteristics and optical properties of plasma assisted reactive magnetron sputtered dielectric thin films for planar waveguide applications," Surf. Coat. Tech. **206**(23), 4930–4939 (2012).
17. D. Ristau and H. Ehlers, "Thin Film Optical Coatings," in *Springer Handbook of Lasers and Optics*(Springer, 2012), pp. 401–424.
18. W. Sellmeier, "Zur erklärung der abnormen farbenfolge im spectrum einiger substanzen," Annalen der Physik und Chemie **219**(6), 272–282 (1871).
19. K. Saitoh, M. Koshiba, T. Hasegawa, and E. Sasaoka, "Chromatic dispersion control in photonic crystal fibers: application to ultra-flattened dispersion," Opt. Express **11**(8), 843–852 (2003).
20. E. K. Akowuah, T. Gorman, H. Ademgil, S. Haxha, G. K. Robinson, and J. V. Oliver, "Numerical analysis of a photonic crystal fiber for biosensing applications," Quantum Electronics, IEEE Journal of **48**(11), 1403–1410 (2012).
21. J. Homola, H. B. Lu, G. G. Nenninger, J. Dostálek, and S. S. Yee, "A novel multichannel surface plasmon resonance biosensor," Sens. Actuators B Chem. **76**(1-3), 403–410 (2001).
22. H. Ditlbacher, N. Galler, D. M. Koller, A. Hohenau, A. Leitner, F. R. Aussenegg, and J. R. Krenn, "Coupling dielectric waveguide modes to surface plasmon polaritons," Opt. Express **16**(14), 10455–10464 (2008).
23. H. Ademgil, S. Haxha, T. Gorman, and F. AbdelMalek, "Bending effects on highly birefringent photonic crystal fibers with low chromatic dispersion and low confinement losses," J. Lightwave Technol. **27**(5), 559–567 (2009).
24. P. Falkenstein and B. L. Justus, "Fused array preform fabrication of holey optical fibers," (Google Patents, 2013).
25. B. T. Kuhlmey, B. J. Eggleton, and D. K. Wu, "Fluid-filled solid-core photonic bandgap fibers," J. Lightwave Technol. **27**(11), 1617–1630 (2009).
26. K. Nielsen, D. Noordegraaf, T. Sørensen, A. Bjarklev, and T. P. Hansen, "Selective filling of photonic crystal fibres," J. Opt. A, Pure Appl. Opt. **7**(8), L13–L20 (2005).
27. A. Schwuchow, M. Zobel, A. Csaki, K. Schröder, J. Kobelke, W. Fritzsche, and K. Schuster, "Monolayers of different metal nanoparticles in microstructured optical fibers with multiplex plasmonic properties," Opt. Mater. Express **2**(8), 1050–1055 (2012).
28. A. Hassani, B. Gauvreau, M. F. Fehri, A. Kabashin, and M. Skorobogatiy, "Photonic crystal fiber and waveguide-based surface plasmon resonance sensors for application in the visible and near-IR," Electromagnetics **28**(3), 198–213 (2008).
29. J. Dostálek, H. Vaisocherova, and J. Homola, "Multichannel surface plasmon resonance biosensor with wavelength division multiplexing," Sens. Actuators B Chem. **108**(1-2), 758–764 (2005).
30. J. Homola, S. S. Yee, and G. Gauglitz, "Surface plasmon resonance sensors: review," Sens. Actuators B Chem. **54**(1-2), 3–15 (1999).
31. M. Nielsen, C. Jacobsen, N. Mortensen, J. Folkenberg, and H. Simonsen, "Low-loss photonic crystal fibers for transmission systems and their dispersion properties," Opt. Express **12**(7), 1372–1376 (2004).

1. Introduction

Surface Plasmon Resonance (SPR) is a key technology employed in analyzing the kinetics of bio molecular events in establishing the presence of biochemical target analytes, enabling in situ, label free and highly sensitive optical sensing in real time [1]. The SPR results from the optical excitation of Surface Plasmon Polariton (SPP). SPPs are oscillations of electron charge densities accompanied by a trans-magnetic (TM) polarized electric field propagating along the metal dielectric interface and exponentially decays into both metal and dielectric regions [2]. The propagation characteristics of the surface plasmon wave is highly sensitive to refractive index variations of the dielectric adjacent to the metal, and as a result, binding of target molecules to the metal surface enables monitoring of background (bulk) and surface (target analyte layer) refractive index changes of the analyte [1, 3]. The SPR is highly promising in applications such as optical filtering and sensing [4, 5]. Moreover, accurate detection of molecular (both biological and chemical) interaction and analysis is required in many multiple disciplines such as medical diagnostics, health, environmental protection and bio-chemical technology [3].

Classical SPR based bio-chemical sensors were focused primarily on using a single channel for sensing purposes and did not take in to account noise (error) causing scenarios such as non-specific analyte binding events, temperature variations and instrumental instability that occur in reality [6]. Demands for more accurate, highly sensitive SPR based bio-chemical sensors capable of multi-analyte sensing prompted research interest and development transition from the bulky Kretschmann prism based configuration with many

#235087 - $15.00 USD Received 23 Feb 2015; revised 13 Apr 2015; accepted 15 Apr 2015; published 5 Jun 2015

moving optical and mechanical moving parts to micron level wave guide based configurations which are portable, adaptable to remote sensing and have better integration capabilities [7]. However, sections of cladding and jacket of the wave guide had to be removed manually before gold layer deposition, thus resulting in structural failures and higher fabrications cost.

Photonic crystal fibers (PCFs) also known as holey fibers, have been around for some time [8, 9]. These fibers can have channels included in their construction in which the gold layers can be applied and the analyte can be accommodated [10, 11]. Their fluidic design capabilities are highly beneficial in applications where volatile or toxic samples are used. In addition, a small amount of samples are required for interactions with the core modes since fluid slot diameters are in micron scale [12].

Present research trend are geared towards all glass fibers using vacuum assisted ingiltration of molten metal phosphates glass in to silica PCF enabling band gap guidance by an external electric field [13].

In this research, we numerically report a multi-channel holey fiber plasmonic biosensor characterized to operate in aqueous environments using numerical computation tool, Finite Element Method (FEM), with anisotropic Perfectly Matched Layers (PML). Our results indicate that our proposed sensor can either be operated in multi analyte detection mode or be used to eliminate effects of environmental noises on sensor results (self-referencing mode). With regards to sensitivity, our proposed SPR biosensor has sensitivities values comparable and even better than those in [3, 14], Qin et al, Dash et al.. A detailed description of the sensor design and numerical modeling is given in the next section followed with an interpretation on the influences of several structural variables on the sensor performance. Finally a summarized conclusion in last section is provided.

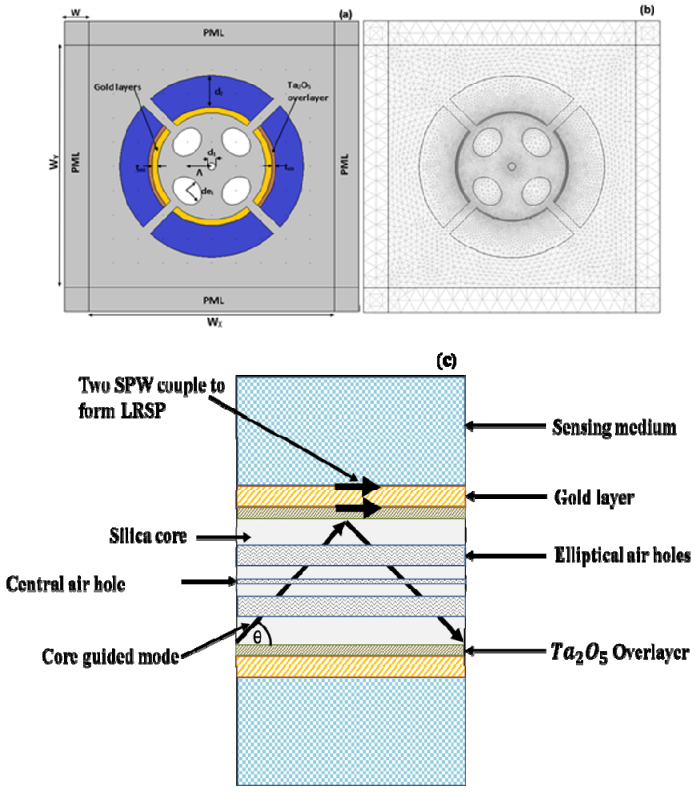

Fig. 1. (a) Schematic of biosensor showing various components.(b)Meshed module for numerical computation. (c) A schematic in, reflection mode, of the experimental setup.

#235087 - $15.00 USD Received 23 Feb 2015; revised 13 Apr 2015; accepted 15 Apr 2015; published 5 Jun 2015

2. Theory

The schematic of our proposed biosensor, illustrated in Fig. 1(a), comprises four micro fluid channels, $d_{2,}$ with a gold layer of thickness $t_{au,}$ on their inner sides. Additionally, a thin high refractive index dielectric over layer, tantalum pent-oxide (Ta_2O_5), of thickness $t_{ao,}$ can be applied on the gold layer using plasma assisted reactive magnetron sputtering in only two channels.

Even though existing physical and chemical methods [15], suggest that Ta_2O_5 has an acceptable slab waveguide loss of ~1 dB/cm, at both visible and infra-red wavelengths, making it ideal for MOF applications [16], ultimately, device sensitivity is lowered as some field energy required to excite a strong enough plasmon for sensing is lost to scattering. Tantalum oxide shows a wide spectral range of high transparency, low losses and a high melting point making stable in comparison to material like ITO or silicon [17].

Furthermore, four elliptical air holes, de_i (i denotes the minor or major axis), that form a low refractive index region for wave guidance and a central air hole, d_1, to tune resonance wave length of the guided mode in order to match that of the plasmon mode. The refractive index of air, n_{air}, is 1.00. Also the analyte refractive index is denoted as n_{a1} for the horizontal micro fluidic slot pair (Channel 1) and n_{a2} for the vertical micro fluidic slot pair (Channel 2). The hole to hole spacing, Λ, is 1.0μm. The background material is pure silica, and is modelled using the Sellmeier equation [18]:

$$n(\lambda) = \sqrt{1 + \frac{B_1\lambda^2}{\lambda^2 - C_1} + \frac{B_2\lambda^2}{\lambda^2 - C_2} + \frac{B_3\lambda^2}{\lambda^2 - C_3}} \tag{1}$$

where n and λ(nm) is the index of refraction and wavelength respectively, $B_{(i = 1,2,3)}$ and $C_{(i = 1,2,3)}$ are Sellmeier coefficients. The values of the coefficients are defined as follows B_1 = 0.696166300, B_2 = 0.407942600, B_3 = 0.897479400, C_1 = 4.67914826 × 10^{-3}μm^2, C_2 = 1.35120631 × 10^{-2} μm^2 and C_3 = 97.9340025 μm^2 [19] and thus the material dispersion, taking into consideration of the effects of both ordinary and extraordinary indices, of the fibre has been accounted for. Gold permittivity is modelled from Johnson and Christy data [20]. Furthermore, the material properties of tantalum pent oxide layer is computed from

$$n_{Ta_2O_5} = 1.88 + 178.4\times10^2/\lambda^2 + 52.7\times10^7/\lambda^4 \tag{2}$$

where λ is the wavelength in nm [21]. Figure 1(b) illustrates the FEM meshed module consisting of 32404 elements with 226997 degrees of freedom. Anisotropic PML is the boundary condition employed in the study for the leaky modes as they travel through the fibre. In addition, it is worth stating that any desired number of modes (confined or leaky) can be determined and analysed by deploying the developed model. Modal analysis is performed on the polarised fundamental modes, HE_{11}^x and HE_{11}^y in the *x*-*y* Cartesian plane as the mode propagates in the *z* direction.

Furthermore, coupled mode theory facilitates the understanding of how the core guided mode couples with the surface plasmon wave. At the resonance point the core guided mode couples with the surface plasmon wave since their propagation constants match, resulting in much loss of energy from the core mode to the plasmon mode [22]. A change in either the resonant wavelength or the intensity of the two modes is the measurable parameter. The imaginary part of the complex refractive index (n_{eff}) is used to determine the occurred confinement losses (L) [23] using:

$$L = 8.686\times\frac{2\pi}{\lambda(\mu m)}\,\mathrm{Im}(n_{eff})\times10^4\,\mathrm{dB/cm} \tag{3}$$

#235087 - $15.00 USD Received 23 Feb 2015; revised 13 Apr 2015; accepted 15 Apr 2015; published 5 Jun 2015

Fabrication of the proposed biosensor should be relatively easy primarily due to the few but large holes. One typical method would be fused array preform fabrication method that can be used to realize air hole diameters of typically 0.1 microns in a uniform and mass reproducible manner [24]. In addition, aqueous samples can be introduced into the slots either with pressure or capillary flow [9, 25, 26]. As there is an absence of a flow cell system, the cross sectional area of the micro fluidic channels would be no concern as moving sample volumes within a time frame at a given pressure won't be required. High pressure chemical vapor technique is one efficient way to apply gold depositions on the inner surfaces of the micro fluidic slots [10]. Both gold and the metal oxide are chemically stable and are relatively easy to come by. Alternatively, nanoparticle layer deposition(NLD) can be used to deposit the required amount of gold [27].

3. Simulation and results

We start our analysis with the investigation of the coupling phenomenon between the core-guided mode and the plasmonic mode. A strong coupling is essential if it's to be harnessed for sensing. For this reason, the air hole lattice arrangement in our biosensor structure facilitates this. Our biosensor is modeled using the following parameters; $\Lambda = 1.0\mu m$, $d_1/\Lambda = 0.30$, $d_2/\Lambda = 1.55$, $de_x/\Lambda = 0.65$, $de_y/\Lambda = 0.50$, $t_{au} = 50nm$, $t_{ao} = 40nm$. Channel 1 and Channel 2 are filled with an aqueous analyte of refractive index, $n_{a1} = 1.33$ and $n_{a2} = 1.34$, respectively. Loss and dispersion values for the two polarized modes, HE_{11}^{x} and HE_{11}^{y} are solved for over 400nm window.

Figure 2 illustrates the loss curve and dispersion relationship between the core guided mode and the plasmon mode at the phase matching wavelengths for *x*-polarized and *y*-polarized fundamental modes. The peaks in the loss curve (thick solid curve) indicate high energy losses of the core mode coupled to the plasmon. At these wavelengths, the two modes couple to one another because they have nearly equal refractive indices and propagation constants hence the core mode couples and resonates with the plasmon mode. The phase matching wavelengths are indicated by the intersection of the plasmon mode dispersion curve (dotted line) and core mode dispersion curve (dash-dot line) located around 675nm and 900nm for the *x*-polarized fundamental. While the *y*-polarized fundamental couples with the plasmon wave at 645nm and 836nm.

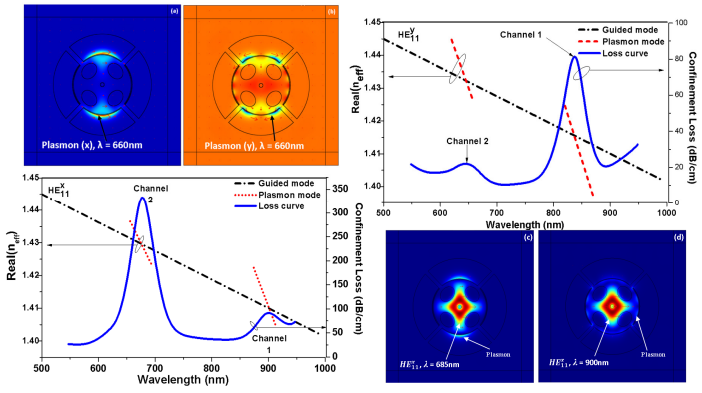

Fig. 2. Loss curve and dispersion relationship between the core guided mode and the plasmon modes at resonant wavelength. For x-polarized and y-polarized fundamental modes. (a) and (b) are magnetic field distributions of plasmon mode.(c)and(d) are magnetic field distributions of core guided mode at the resonance wavelength.

Figure 2 illustrates magnetic field profiles of plasmon waves on the surface of the metal for both the *x* and *y* polarized fundamental modes (inserts (a) and (b)). This explains the high

#235087 - $15.00 USD Received 23 Feb 2015; revised 13 Apr 2015; accepted 15 Apr 2015; published 5 Jun 2015

losses occurred at those wavelengths. Fundamental modes exhibit different degrees of the core guided mode leaking to the plasmon mode. This depends on which mode has closer interaction with the plasmon. Inserts (c) and (d) illustrates the magnetic field distributions of HE_{11}^{x} at both phase matching wavelength of 685nm and 900nm. It is worthy to note that there is more leakage at the 685nm point as compared to the 900nm point.

Furthermore, Figure 3(a) shows field data for the guiding modes for longer wavelengths covering the second peak. Figure 3(a) shows dispersion plots of our sensor with and without a metallized surface to support the plasmon for both *x* and *y* polarized fundamentals. It can be observed that the effective indices of the fundamental polarized modes for both setups are in close proximity, which is crucial for coupling of the core guided mode to the plasmon mode at resonance [20].

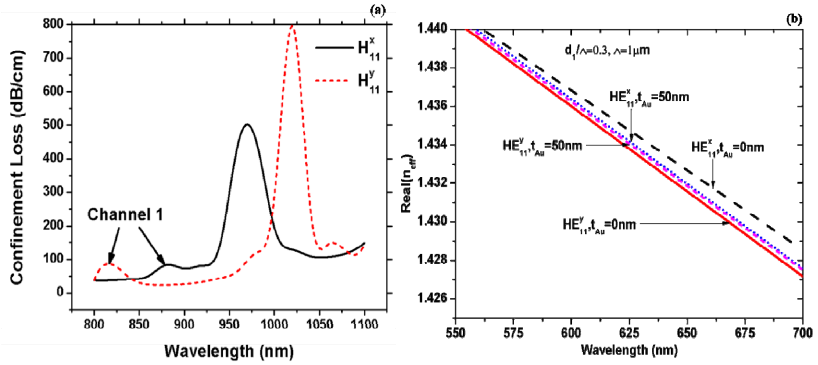

Fig. 3. Dispersion relationship of fundamental mode with and without a layer of metal.

3.1 Biosensor characterization in multi analyte sensing mode

We further investigate the potential of the proposed biosensor for multi analyte sensing. In a first run, Channel 1 and Channel 2 are filled with aqueous analytes with refractive indices, n_{a1} = 1.33 and n_{a2} = 1.34, respectively, whilst maintaining the same structural parameters as previously used. The second run is made with different set of refractive indices, n_{a1} = 1.34, and n_{a2} = 1.35. The confinement loses of both polarized modes (HE_{11}^{x} and HE_{11}^{y}) are obtained for each run. Figure 4 illustrates the simulation results obtained from the two runs, in the form of spectra loss plots for HE_{11}^{x} and HE_{11}^{y} modes.

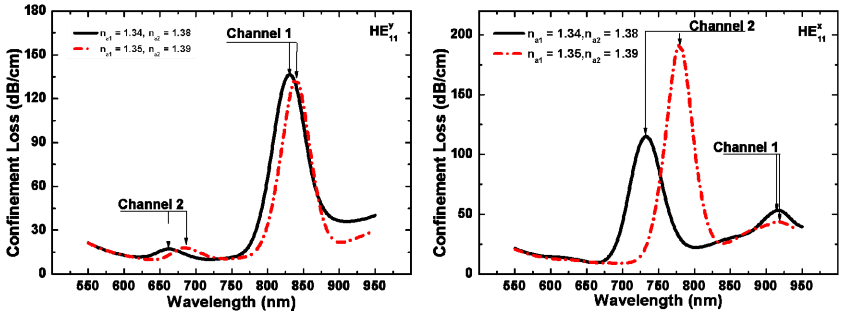

Fig. 4. Multi analyte operation of biosensor showing loss spectra of x and y polarizations of the fundamental modes (HE_{11}^{x} and HE_{11}^{y}). Attenuation peaks correspond to excited plasmons on the gold surface. The change of line type correspond to change in analytes in both runs.

Two peaks are observed to occur in the loss curves. The coupling of the core guided mode to the plasmon mode occurs at two resonance wavelengths because of the presence of two

#235087 - $15.00 USD Received 23 Feb 2015; revised 13 Apr 2015; accepted 15 Apr 2015; published 5 Jun 2015

different analytes. The shift in the loss curves for each polarized fundamental mode is attributed to the change in the analyte refractive used in both runs. As the surface plasmon is sensitive to changes in the analyte refractive index, the phase matching points vary as such. The bulk and surface refractive index change can be monitored using this method.

3.2 Biosensor characterization in self-referencing mode

To determine the potential of the metallized biosensor to operate in self-referencing mode, the n_{a1} is fixed at 1.33 in Channel 1 while n_{a2} is varied from 1.32 to 1.36 in Channel 2 without altering any other structural parameters. As can be seen from Fig. 5, the variation of the analyte refractive index in Channel 2 causes the peaks to shift towards longer wavelengths while no shifts are detected for Channel 1 containing the fixed analyte. This happens for both HE_{11}^{x} and HE_{11}^{y} modes. The distinguishing feature is the change of the much lossy Channel 2 of the HE_{11}^{x} mode to the Channel 1 in HE_{11}^{y}. This is attributed to stronger coupling of HE_{11}^{x} mode to plasmon mode in Channel 2 than Channel 1 whilst HE_{11}^{y} couples better with the plasmon in Channel 1 than Channel 2.

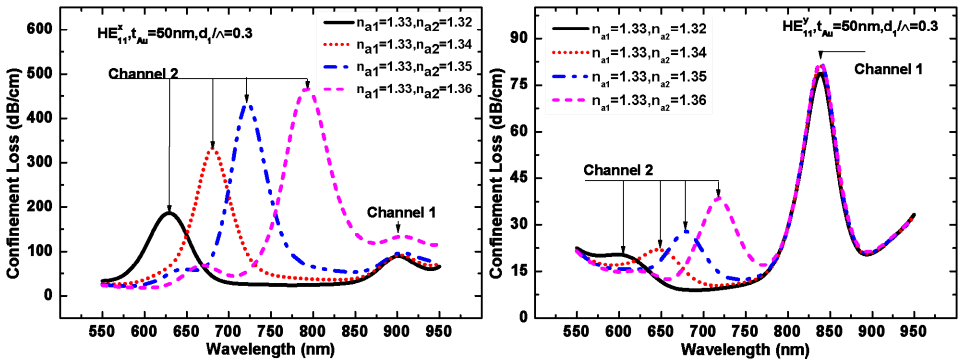

Fig. 5. Self-referencing operation of biosensor showing loss spectra of x and y polarizations of the fundamental modes (HE_{11}^{x} and HE_{11}^{y}).

3.3 Tuning of plasmon excitations

The proposed PCF biosensor is very sensitive to changes when its structural key parameters are varied. Its operation can be further optimized by fine tuning of these parameters. This section expounds on the influences of four structural variables, namely, the central air hole, d_1/Λ, the elliptical cladding air hole, de_i/Λ, thickness of gold layer, t_{au}, and over layer thickness, t_{ao}. When each investigation of the effect of a structural variable is carried out, all other structural variables are kept as they were first defined.

The core guided mode is pushed outwards and its presence increases near the metal layer as d_1/Λ is varied from 0.25 to 0.35, resulting in increasing mode loss to the surface plasmon and shifting of the resonance peaks to longer wavelengths. Figures 6(a) and 6(b), illustrates the effects of d_1/Λ on mode loss for HE_{11}^{x} and HE_{11}^{y}. In addition, the dispersion plots, Fig. 6(c) shows a general decrease in the refractive indices.

#235087 - $15.00 USD Received 23 Feb 2015; revised 13 Apr 2015; accepted 15 Apr 2015; published 5 Jun 2015

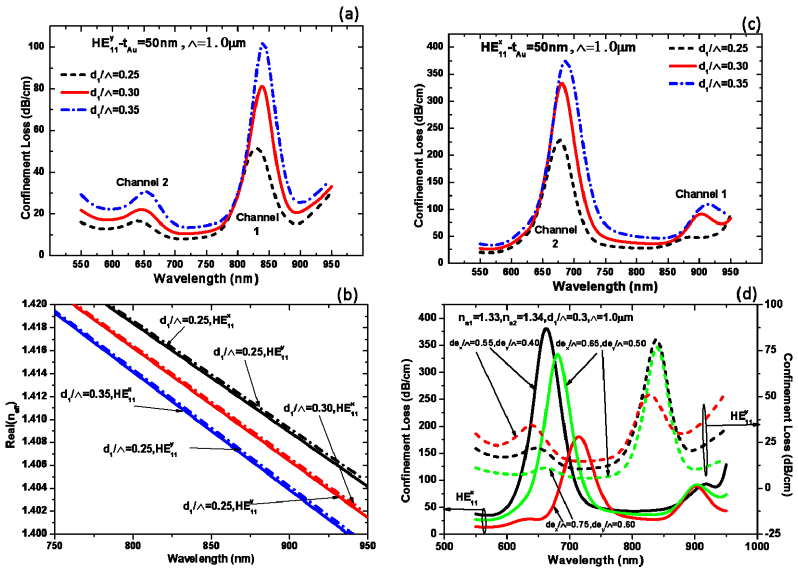

Fig. 6. Dependence of resonance peak wavelength on central air hole for HE_{11}^{x} and HE_{11}^{y} (inserts (a) and (c)). Insert (b) displays dispersion trend for varying central air hole for HE_{11}^{x} and HE_{11}^{y} .Result on display are for the biosensor operating in self-referencing mode.

Furthermore, the core guided mode is effectively shielded and its presence decreases near the metal layer as de_x/Λ and de_y/Λ is varied from 0.55 to 0.75 and 0.40 to 0.60, respectively, resulting in decreasing mode loss (Channel 2) to the surface plasmon and shifting of the resonance peaks to shorter wavelengths. Figure 6(d) illustrates the effects of de_x/Λ and de_y/Λ on mode loss.

Referring to the fact that surface plasmon modes are metal surface phenomena, we can predict that there is a strong relation between them. We investigate this by varying t_{au} from 45nm to 55nm with Channel 1 and Channel 2, containing aqueous samples of refractive indices 1.33 and 1.34, respectively. Figures 7(a) and 7(b) shows the loss curves with peaks shifting to longer wavelengths and decreasing guided mode losses (as guided mode is shielded more from plasmon) for each variation of t_{au} for Channel 2, nonetheless an inverse for Channel 1. The presence of a high refractive index over layer in Channel 1 converts the shielding effect to a magnifying one inducing a stronger plasmon supported by the thickening gold layer, hence stronger coupling and larger mode loss. Such a relation provides an opportunity for the study of metal surface particle activities at nano-scale level [28].

We further investigate the effect of over layer thickness on modal loss as t_{ao} is varied from 20nm to 60nm. Figure 7(a) illustrates an exciting phenomenon where modal losses decrease as t_{au} increased in channel 1. Interestingly as t_{au} approaches a 100um, the core mode is effectively confined to the core of the PCF and channel one begins to exhibit modal loss decrease as t_{au} increases similar to channel 2. Figure 7(c) shows changes in modal loss of Channel 1 and with no plasmon peak shifts for both fundamental HE_{11}^{x} and HE_{11}^{y} modes. It shows a general decrease in modal loss in Channel 1 as t_{ao} is varied. The shift in the loss curves in channel 1 for each polarized fundamental mode is attributed to the change gold thickness (t_{au}) . The degree of strength of the coupling between the core guided mode and the surface plasmon is sensitive to t_{au} changes, the phase matching points vary as such.

#235087 - $15.00 USD Received 23 Feb 2015; revised 13 Apr 2015; accepted 15 Apr 2015; published 5 Jun 2015

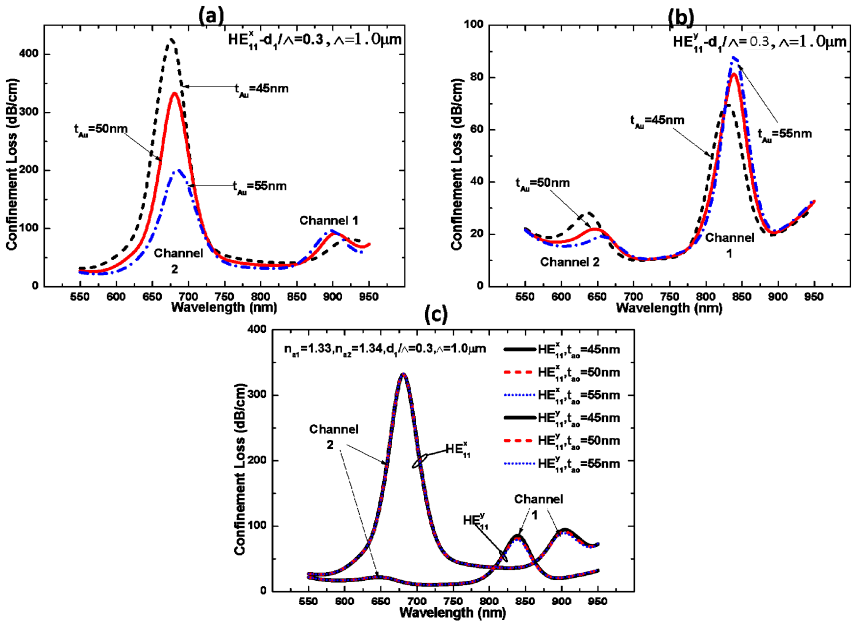

Fig. 7. Effect of variation of gold thickness on loss for proposed PCF biosensor operating in self-referencing mode (inserts (a) and (b)) for HE_{11}^{x} and HE_{11}^{y} modes. The dependence of loss spectra on overlay thickness is also displayed in insert (c).

The proposed multi channel sensor structure has the potential to perform various measurements that would allow for automatic calibration and error detection especially in self-referencing mode. This provides a more practical approach of keeping the operational accuracy of the sensor at a maximum as the automatic calibration can easily be performed as often as is necessary in comparison to [6], Zhang et al.

3.4 Characterization of sensor sensitivity

The sturdy dependence of the surface plasmon wave on the analyte refractive index is the underlying principle used by most sensors to detect changes. The variation of the analyte refractive index causes an associated shift in the resonance wavelength. Both bulk and surface refractive index changes contribute to the shift of the resonance wavelength [29]. Analysis of the resonant wavelength shifts can be performed in two methods; intensity or amplitude interrogation and wavelength or spectral interrogation. The degree of discrimination in wavelength or intensity determines the level of sensor sensitivity.

Amplitude interrogation in comparison to wavelength interrogation is more economical and more easily implemented [30]. However its low sensing capability and small range of operation make wavelength interrogation a better choice in that respect. Mathematically, amplitude sensitivity can be represented as

$$n_A(\lambda) = -(\partial\alpha(\lambda, n_a)/\partial n_a)/\alpha(\lambda, n_a) \text{per refractive index units} \left[\text{RIU}^{-1}\right] \qquad (4)$$

$\alpha(\lambda, n_a)$ represents lost energy of the core mode as at a particular wavelength [25]. As illustrated in Fig. 8, the biosensor operating in self-referencing mode recorded typical sensing values of 425 RIU^{-1} and 131 RIU^{-1} for both HE_{11}^{x} and HE_{11}^{y} modes, respectively, with t_{au} = 45nm. This resolves to resolution values of 2 × 10^{-5} RIU and 7 × 10^{-5} RIU for *x* and *y* polarized fundamental modes in self-referencing mode assuming a reliable detection of 1% change in intensity is made in both modes.

#235087 - $15.00 USD Received 23 Feb 2015; revised 13 Apr 2015; accepted 15 Apr 2015; published 5 Jun 2015

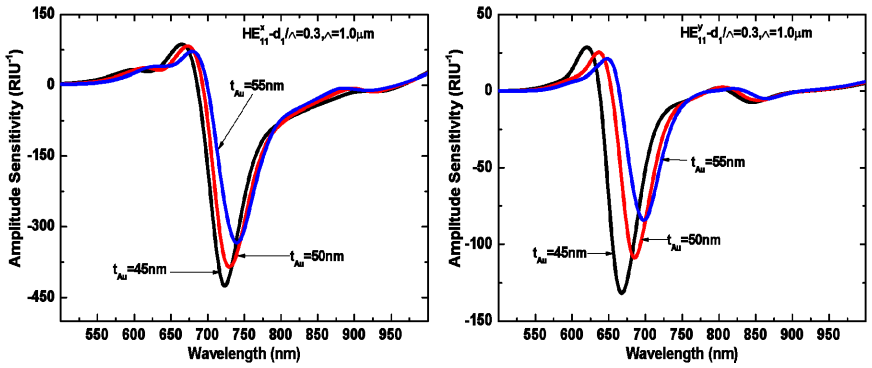

Fig. 8. Relationship between amplitude sensitivity and gold layer thickness of the PCF biosensor for varying t_{Au}.

Furthermore, one can notice from Fig. 8, that amplitude sensitivity is inversely related to t_{au}. This is because as the gold layer thickens, it blocks more of the leakage of the core guided mode to the plasmon mode weakening the coupling between the two resulting in lower sensitivities. The stronger presence of the *x* polarized fundamental mode near the gold layer is responsible for the higher sensitivity value for it as compared to the *y* polarized mode at t_{au} = 45nm.Moreover, wavelength interrogation is applied to the proposed biosensor operating in both multi-analyte and self-referencing modes to characterize its sensing capability. Spectral interrogation is define mathematically as

$$S_\lambda(\lambda) = \frac{\partial \lambda_{peak}}{\partial n_a} \quad [\mathrm{nm/RIU}] \tag{5}$$

λ_{peak} is the wavelength at which the loss peaks occur. The biosensor operating in multi-analyte mode has the largest $\partial\lambda_{peak}$ of 46nm (Channel 2) and 23nm (Channel 1) for HE^x_{11} and HE^y_{11} occurring when t_{au} = 50nm resulting in spectral sensitivities of 4600nm/RIU and 2300nm/RIU respectively. Assuming a reliable detection of 0.1nm change in the resonance position, typical sensor resolutions of 2×10^{-5}RIU and 4×10^{-5}RIU are made in both modes, respectively. Considering the fact that the biosensor is operating in self-referencing mode, maximum $\partial\lambda_{peak}$ values of 41nm (Channel 2) and 33nm (Channel 2) are recorded for HE^x_{11} and HE^y_{11} occurring when t_{au} = 50nm, resulting in spectral sensitivities of 4100nm/RIU and 3300nm/RIU, respectively. Assuming a reliable detection of 0.1nm change in the resonance position, typical sensor resolutions of 2×10^{-5}RIU and 3×10^{-5}RIU are made in both modes, respectively.

Figure 9 shows the loss peaks and the wavelengths at which they occur as t_{au} is varied from 45nm to 55nm for both operational modes.

In general, illustrated results show that changes in the refractive index of the aqueous samples in either channels causes the resonant wavelength to shift to longer wavelengths.

Sensor length plays a major role in sensor response. Sensors with large lengths are easy to fabricate and have sufficient interaction with the aqueous sample as compared to sensors with small lengths [6]. The better the interaction, the better the sensor response. The length of the proposed biosensor is restricted to the centimeter scale in order to achieve a good balance between sensor sensitivity and ease of fabrication.

Even though scaling up would reduce the burden during fabrication it would compromise on the sensitivity of the biosensor as there would be a weaker interaction between plasmon and core mode with the single mode degenerating into a multimode.

#235087 - $15.00 USD Received 23 Feb 2015; revised 13 Apr 2015; accepted 15 Apr 2015; published 5 Jun 2015

The guiding property in such hollow core PCF is only determined the diameter to spacing ratio(d/Λ) . For d/Λ<0.30 the fibre is single mode for all wavelengths. Thus, for a fixed wavelength propagation losses limit the scaling up of the mode field diameter [31]. In addition a higher powered light source would be required to achieve better sensitivity results.

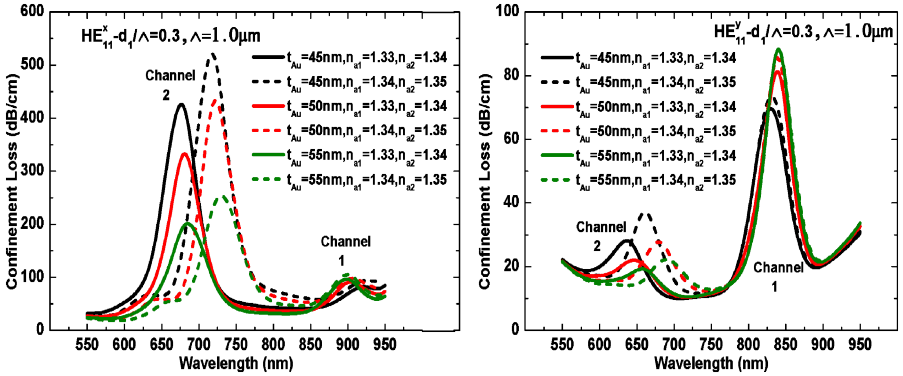

Fig. 9. Resonant wavelength dependence on gold thickness and analyte refractive index.

4. Conclusion

A comprehensive theoretical analysis of holey SPR based biosensor is expounded in this paper. The biosensor schematic comprises microfluidic channels, wave-guide elliptical air hole lattice, and high refractive index over layer and metallized layers making this design densely compact and amenable to integration, in contrast to other common SPR biosensors.

The large sized air holes and fluidic channels of the biosensor would facilitate aqueous sample loading with pressure or capillary action [9, 25, 26] and the fabrication of the holes using fused array preform fabrication method that can be used to realize air hole diameters of typically 0.1 microns [24]. The thin gold layer on the inner surfaces of the micro fluidic slots can be achieved using high pressure chemical vapour technique [10]. Alternatively, electrolytic plating can be used to deposit the required amount of gold [11, 12].

The proposed biosensor design enables configurability to operate in two modes; multi analyte sensing mode and in self-referencing mode. The operation of the biosensor in multi analyte mode enables detection of two analytes in one aqueous sample. It can also be used in the identification of two different liquid samples each containing a different analyte. Similarly, self-referencing operation mode eliminates external influences (instrumental noises variation of non-target analytes, and temperature fluctuation).

The coupling conditions at resonance, sensitivity, and loss spectra of this SPR based PCF biosensor has been investigated using a finite element method and perfectly matched layered boundaries. It has been demonstrated that the PCF design structure can operate in two modes and measure different sensitivities for each fundamental mode (HE^x_{11} and HE^y_{11}). The reported biosensor, in multi analyte operation, mode has characteristic sensor resolution values of 2×10^{-5}RIU and 4×10^{-5}RIU for HE^x_{11} and HE^y_{11} modes, recorded for the spectral interrogation mode. On the other hand, in self-referencing operational mode, characteristic sensor resolution values of 2×10^{-5}RIU and 3×10^{-5}RIU for HE^x_{11} and HE^y_{11} modes are recorded for the spectral interrogation mode whilst 2×10^{-5} RIU for HE^x_{11} mode and 7×10^{-5} RIU for HE^y_{11} modes when the amplitude interrogation mode is performed.

#235087 - $15.00 USD Received 23 Feb 2015; revised 13 Apr 2015; accepted 15 Apr 2015; published 5 Jun 2015

In comparison to similar bi-functional sensor designs as reported in [6], Zhang et al, our proposed design multi analyte mode demonstrates a sensitivity values of 4600nm/RIU and 2300nm/RIU which is better in comparison to 1535nm/RIU for Channel 1 and 1550nm/RIU for Channel 2 and 3 reported in [6], Zhang et al.

A maximum sensitivity value of 4600nm/RIU, in multi analyte detection mode, is recorded by our proposed sensor which is better in comparison to a maximum of 4240nm/RIU reported in [3, 14], Qin et al, Dash et al. Furthermore, in self-referencing operational mode, a maximum sensitivity value of 4100nm/RIU is demonstrated which is comparable to maximum of 4240nm/RIU reported in [3, 14], Qin et al, Dash et al.

#235087 - $15.00 USD Received 23 Feb 2015; revised 13 Apr 2015; accepted 15 Apr 2015; published 5 Jun 2015